Nuclear Instruments and Methods in Physics Research A 619 (2010) 190–197

Contents lists available at ScienceDirect

Nuclear Instruments and Methods in Physics Research A

journal homepage: www.elsevier.com/locate/nima

Optimisation of the spatial linearity in backgammon-type multi-wire gas proportional counters—The relevance of charge cloud distribution

A.T. Payne [a,*], J.A. Kimpton [b], L.F. Smale [a], C.T. Chantler [a]

[a] School of Physics, University of Melbourne, Parkville, Victoria 3010, Australia
[b] Australian Synchrotron, 800 Blackburn Road, Clayton, Victoria 3168, Australia

ARTICLE INFO

Available online 21 December 2009

Keywords:
Spatial linearity
MWPC
Detector modelling
X-ray spectroscopy

ABSTRACT

The backgammon-type multi-wire gas proportional counter (MWPC) enables the detection of X-ray photons in two dimensions with a high degree of spatial linearity. An accurate simulation of the detector geometry is developed to further optimise the spatial linearity achievable, by modelling the ideal linear output and through mapping of the experimental residual signature. Three models are presented, each achieving considerable improvements on key linearity measures over previous work, and providing strong evidence for the dependence on charge cloud distribution. Linearity to micron levels across 24 mm are demonstrated for MWPCs.

1. Introduction

The science of spectroscopy requires precision instrumentation capable of highly linear and spatially resolved response. X-ray spectroscopy additionally requires linearity with respect to energy and intensity, and hence the ability to accurately resolve spectra by energy is paramount.

Since the invention of the multi-wire gas proportional counter (MWPC) by Charpak in 1968 [1], proportional counters have been of fundamental importance not only to the fields of nuclear and elementary particle physics, for which they were developed, but to many other areas such as X-ray spectroscopy, protein crystallography, and medicine [2–5]. The ability of such devices to provide fundamental insight into so many fields of science, eventually led to the award of the 1992 Nobel Prize in Physics to Charpak, 'for his invention and development of particle detectors, in particular the multiwire proportional chamber'.[1]

At the University of Melbourne, high precision tests of Quantum Electrodynamics (QED) have been undertaken using a Johann-type curved crystal spectrometer coupled to an Electron Beam Ion Trap (EBIT) [2,6]. The EBIT produces highly charged ions, uncontaminated by other elements or charge states, and greatly limits thermal and Doppler broadening effects through cooling and confinement. Increased efficiency is achieved by curved crystal focussing, and the use of gravity-referenced inclinometers allows measurement of the diffraction angle to arcsecond resolution. The backgammon-type MWPC is an integral part of this system with advantages due to its large active detection area, spatial linearity and high efficiency over a range of energies. By contrast, other detector types have good resolution, but the large range of X-ray energies leads to highly variable efficiencies, and restricted detection area. Using this spectrometer system, experimental measurements of atomic transition energies result in fractional uncertainties in energy as low as $(2-4)\times10^{-5}$ [2].

Recently, multi-wire proportional counters have been reduced in scale and embedded upon a solid matrix to yield multi-strip detectors [7–9] and multilayer printed circuit boards [10]. These latter designs use different physics and different cascade and recombination processes, but fundamentally have the same characteristics in terms of image formation and defect analysis, and hence have very similar functionality regarding sources and characterisation of non-linearities. A general discussion of some key noise limits for these types of detectors has been made, which certainly indicates some key limitations in potential statistical information and hence resolution or linearity [11]. Recent publications have observed very large spatial non-uniformities which can relate to the subject of this investigation [12]. Further new devices are being developed and linearity and resolution are key parameters in their utility, often limited by either charge cloud deposition or non-linearities as discussed [13,14]. However, under ideal circumstances these limitations may be overcome, to reveal intrinsic non-linearities due to limitations of board design which simple charge division approaches do not predict.

A simulation has been developed which accurately describes the internal geometry of the backgammon-type MWPC and has assisted in the identification and minimisation of several sources of non-linear detector output. Fig. 1 illustrates the high degree of

* Corresponding author. Tel.: +61 413718475.
E-mail address: apayne@ph.unimelb.edu.au (A.T. Payne).

[1] Presentation speech by Professor Carl Nordling of the Royal Swedish Academy of Sciences, translation from the Swedish text.

0168-9002/$ - see front matter © 2009 Elsevier B.V. All rights reserved.
doi:10.1016/j.nima.2009.12.022

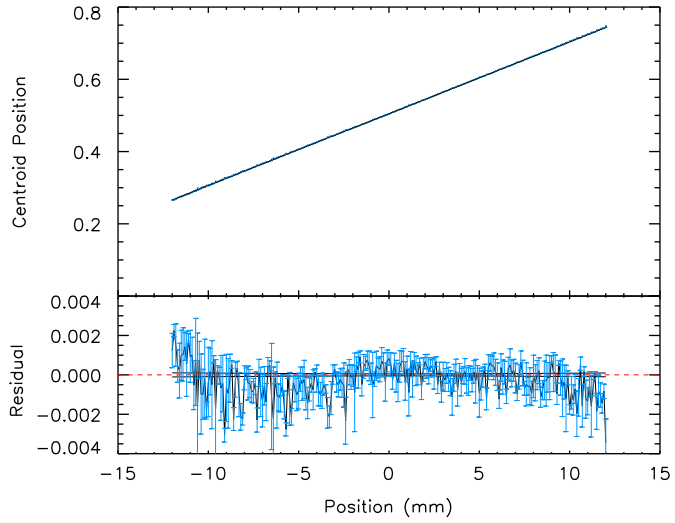

Fig. 1. Fractional centroid position across the detector. Error bars are the standard percentage errors in the determined centroid position. The solid lines are the standard error envelope of the determined linear fit.

spatial linearity obtainable with this detector following these recent developments [15]. Whilst dramatic improvements have been made to linearity measures, unresolved structure still exists within the residual from the linear fit as shown. The work herein further improves the linearity achievable with the backgammon-type MWPC, through an accurate modelling of the detector to show ideal linear output, and through mapping of the experimental residual signature.

2. Detector operation and modelling

2.1. Detector operation

In a MWPC, the source of electrons and ions is the fill gas, which is ionised by an incoming X-ray, and separated by an applied electric field. Through optimisation of parameters such as gas composition, pressure and bias voltage, a counter can be successfully operated in the proportional region whilst maximising spatial resolution.

The detector configuration considered herein is a development on the 'jeu-de-jacquet' or backgammon-type X-ray detector [16], and is described in detail elsewhere [15,17].Two dimensions of position sensitivity are possible with the backgammon-type MWPC, one (coarse) dimension of resolution from the resistive charge distribution of electrons collected along the serpentine anode wire, the other (higher resolution dimension) from the capacitive charge distribution of positive ions collected on the two plates of the backgammon board (Fig. 2). It is this higher resolution dimension which is aligned with the plane of dispersion when the detector is operated as part of the curved crystal spectrometer.

The electronics and data acquisition system (DAQ) employed in the operation of the backgammon-type MWPC are described in full elsewhere [18].

2.2. Detector modelling

An accurate geometrical representation of the MWPC elements was constructed and used as the basis for all simulations. The model accurately reproduces the four output signals (i.e. the two anode signals A and B, and two cathode signals C and D) of the actual detector for an X-ray incident at any cartesian coordinate

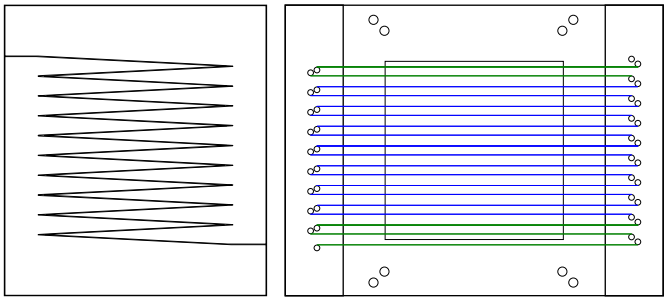

Fig. 2. Shows the backgammon cathode board (left) as divided into two capacitor plates with 100 μm channel separation. The anode wire configuration (right) is shown configured for previous work with the detector [15].

(x,y) within the proportional chamber, hence mapping $(x,y)\longrightarrow(x'(C,D),y'(A,B))$.

Along the anode sensitive dimension, an event within the active region of the detector drifts towards an anode segment, locating the centroid of avalanche formation. As the resistance of the wire is proportional to length, the distance to each end of the anode wire is calculated, and the reciprocals used as the signals A and B to determine the resistive charge division: $y'=A/(A+B)$, where $y'\in t[0,1]$.

In the cathode dimension, the model works by generating a mesh of triangles to represent the geometry of the backgammon board, described as the vertices of polygons. An incident X-ray event is represented by a rectangular distribution of ions surrounding the location of avalanche formation. The radius of this distribution reflects changes in the footprint size. A projection of each charge distribution is made onto the mesh of triangles, and the projected area calculated, proportional to the charge deposited on each side of the backgammon board (defining signals C and D). The position along the cathode axis x', is then determined by capacitive charge division: $x'=C/(C+D)$, where $x'\in[0,1]$.

This model has allowed the determination of the cause of a number of non-linear effects observed experimentally in previous MWPC detector designs [19,20]; leading to major improvements to detector configuration and operation [15]. In this current work, the role of the detector simulation is to show ideal linear output, leading to greater understanding of the residual signature, and hence further improve the spatial linearity response of the detector.

2.3. Detector linearity

An important attribute of the backgammon-type MWPC is its spatial linearity over a large area. Prior to testing the spatial linearity, a set of optimised operating conditions (gas composition, pressure and anode bias voltage) was determined. The MWPC was filled with xenon–methane (10% methane in xenon) at 1.91 atm and operated with an anode bias voltage of 2400 V. To test the spatial linearity, a MacScience rotating anode X-ray source was employed to produce a copper spectrum, monochromated to CuKβ by a Si(1 1 1) channel-cut crystal. Four hundred CuKβ characteristic spectra were collected in 100 μm steps along the axis of cathode sensitivity across the 40 mm window of the detector. Positioning of the MWPC was achieved by a 0.1 μm resolution linear stage, with typical on-axis accuracy of 3 μm and uni-directional repeatability of 0.7 μm.

Each CuKβ spectrum was fitted using the sum of two Lorentzian profiles by a Levenberg–Marquardt least squares algorithm, the centroid determined and compared with the detector position on the linear stage. Fig. 1 illustrates the resulting

spatial linearity with residual from a linear fit. Standard errors in the determination of centroid position are shown as error bars, while the standard error envelope of the linear fit is shown in solid lines.

2.4. Linearity modelling

In order to model the ideal spatial linearity of the MWPC, 400 straight line X-ray distributions incident vertically across the entire active region of the detector were simulated. A Levenberg–Marquardt least squares algorithm was employed to perform a linear fit and reproduce the ideal linear output of the detector for a particular charge footprint.

Fig. 3 shows the fractional residuals for a typical circular charge footprint for CuKβ radiation. The top graph shows the linear residual for both the experimental data and the model (smooth line). The lower graph shows the experimental residual from the model. Error bars are the standard percentage errors in the determined centroid position. The solid lines are the standard error envelope on the determined model fit.

Residuals (Fig. 3) reveal numerous regions across the detector face that deviate from perfectly linear response. For example, the extreme few millimetres at each side of the active detector region demonstrate a strong trend away (in opposing directions) from a straight line response. The detector model closely emulates the experimental data in these regions, a strong implication of a geometrical cause to the observed departures from linearity.

2.5. Geometrical analysis

An initial analytical study of the circular ion cloud projection onto the backgammon board was performed to gain an understanding of the geometrical and physical cause of the observed residual structure. The projected area of the charge cloud determines the cathode signals, hence the charge collected is expected to contain a functional form similar to that for the area (A) of a chord segment:

$$A(r,\theta)=\frac{r^2}{2}[\theta-\sin\theta] \quad (1)$$

where r is the circle radius and θ the central angle. The centre of avalanche formation and hence centre of each ion cloud projection is necessarily in line with an anode wire segment. A general analytical function for each cathode signal then becomes a sum of positive and negative chord areas for each backgammon segment projected onto, summed over each anode wire.

The derivative with respect to θ of the chord area elements (Eq. (2)) highlights the sensitivity of the geometrical model to the centre of an ion cloud passing over the interface between backgammon segments (due to the $[1-\cos\theta]$ dependence). For small ion cloud radii, the design of the MWPC is not adversely effected by this sensitivity as each anode wire intersects the boundary of the backgammon segments only at its midpoint. However, as an ion cloud radius becomes appreciably larger than the pitch of the backgammon teeth, the number of chords forming central angles approaching π radians also increases. This cloud radius is of course energy dependant, but is slowly varying.

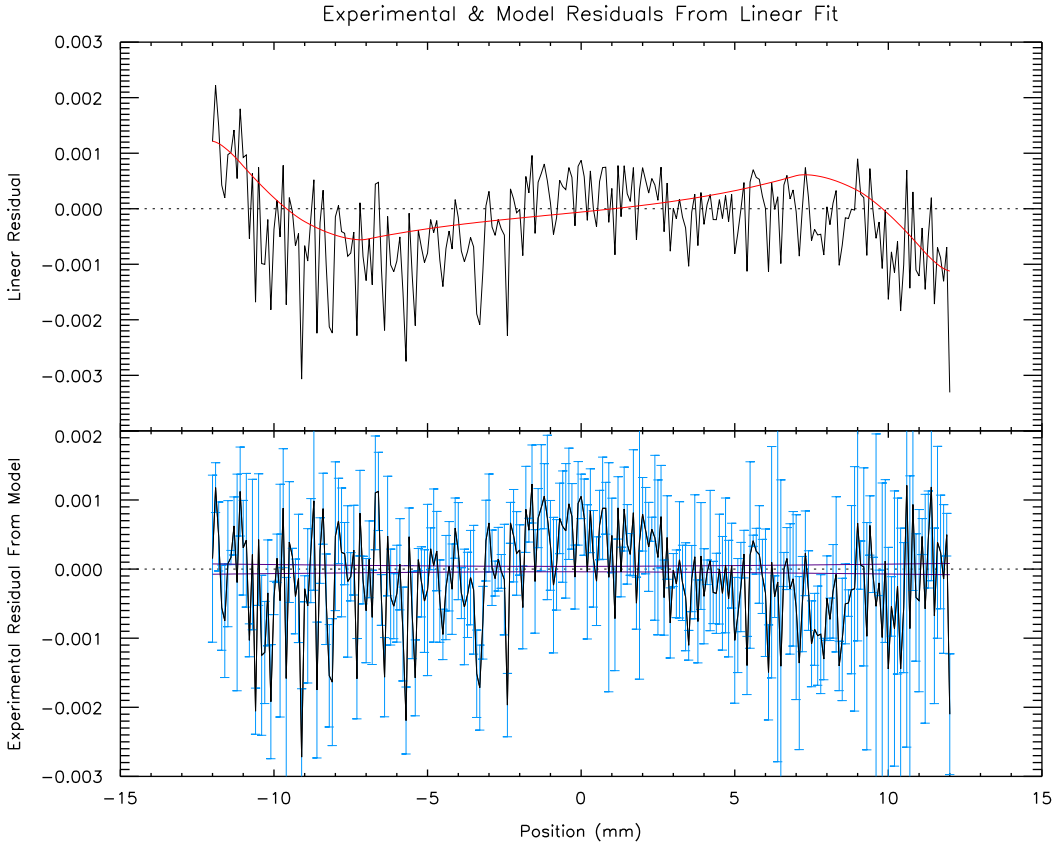

Fig. 3. Shows the fractional residuals for the optimised circular charge footprint with radius of about 8 mm. The top graph shows the linear residual for both the experimental data and the model (smooth line). The lower graph shows the experimental residual from the model. Error bars are the standard percentage errors in the determined centroid position. The solid lines are the standard error envelope on the determined model fit.

The resulting effect to detector response can be the departures from ideal linearity observed both in experiment and simulation

$$\frac{\partial A(r,\theta)}{\partial \theta} = \frac{r^2}{2}[1-\cos\theta]. \quad (2)$$

3. Analysis of models and measures of linearity

The reduced chi-squared of the experimental data fitted with each detector model is a key indicator of model performance:

$$\chi_r^2 = \sum_{i=1}^{N_y} \frac{w_i(y_i-f_i)^2}{N_y-N_p} \quad (3)$$

where y_i are the experimental values to be fitted, f_i the model values, w_i are the weighting values determined by counting statistics as $1/\sqrt{N}$, N_y the number of values, and N_p the number of fitting function parameters.

Fig. 4 shows the χ_r^2 of the model fit to the experimental data over the parameter space of circular ion cloud radius. The dashed line shows the χ_r^2 for the best linear fit to the experimental data ($\chi_r^2 = 3.08$), therefore any point below this threshold represents an improvement in fit of the data and the minimum χ_r^2 the best set of parameters. These ideal model outputs can then be subtracted from the data to form a residual, which is then fit with a linear function by a Levenberg–Marquardt least squares algorithm, and measures of spatial linearity may then be ascertained.

The fractional uncertainty on the fitted gradient ($\Delta m/m$) and offset ($\Delta c/c$) are useful measures of spatial linearity describing the diagonal elements of the uncertainty in the determined fit parameters. This measure does not discriminate between the models presented but instead yields an indication of potential consistency of results for the interpreted or determined scaling. For these optimised models, $\Delta m/m = 0.0196\%$ and $\Delta c/c = 0.00547\%$.

The 'percentage maximum error of the fit' is a good indication that, subject to noise and statistics, a broad feature or wide separation of peaks (of several pixels or resolution elements) can be resolved or determined to very high accuracy. The standard error of each fit is then,

$$\sigma_f^2 = \sum_{i,j} \mathrm{covar}(p_i,p_j)\chi_r^2 \frac{\partial f}{\partial p_i}\frac{\partial f}{\partial p_j} \quad (4)$$

where $i,j \in [1 \ldots N_p]$, p_i and p_j are the fitting parameters, f is the fitting function, and covar (p_i, p_j) is the covariance matrix of the fitted parameters. The percentage maximum error of the fit then is simply the maximum of σ_f expressed as a percentage of the full detector range including the inactive region (40 mm). With better statistics, or perhaps longer counting times, the random noise component of this is reduced arbitrarily, and the resulting measure looks at the intrinsic significance of non-linearity excursions from a well-defined line.

The 'average deviation from fit' is defined as the mean deviation of the detected centroid positions from the linear fit. This is a useful measure of spatial linearity, looking at the typical point-wise excursions over the operational area and estimating the error of a single channel position determination. This measure, however, is affected by limited statistics, but in the absence of statistical limits will provide a strong measure of point-wise departures from linearity.

We define a 'regional differential non-linearity' as the mean of the experimental residual from the model after box-car filtering over 11 points (1.1 mm). In this way much of the random experimental noise is suppressed, leaving a good representation of the typical excursion of the detector from the fit. It provides a very useful measure of the scatter present within a local region across the full active detection range.

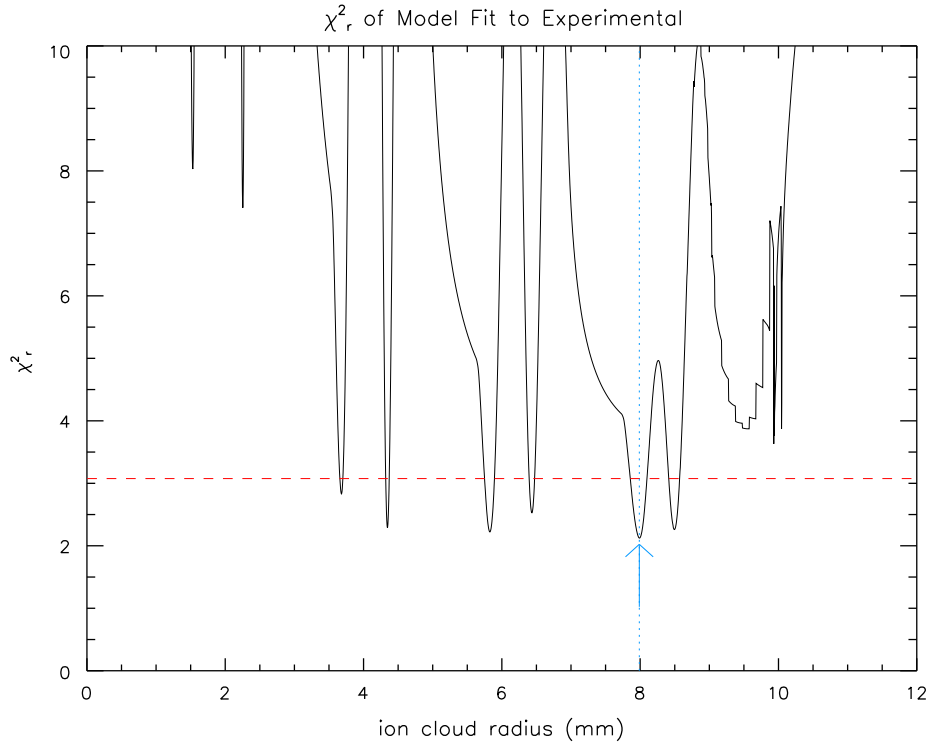

Fig. 4. Shows the χ_r^2 of the circle model fit to the experimental data over the parameter space of ion cloud radius. The arrow highlights the minimum χ_r^2 (2.06) for an ion cloud with an apparent radius of about 8 mm.

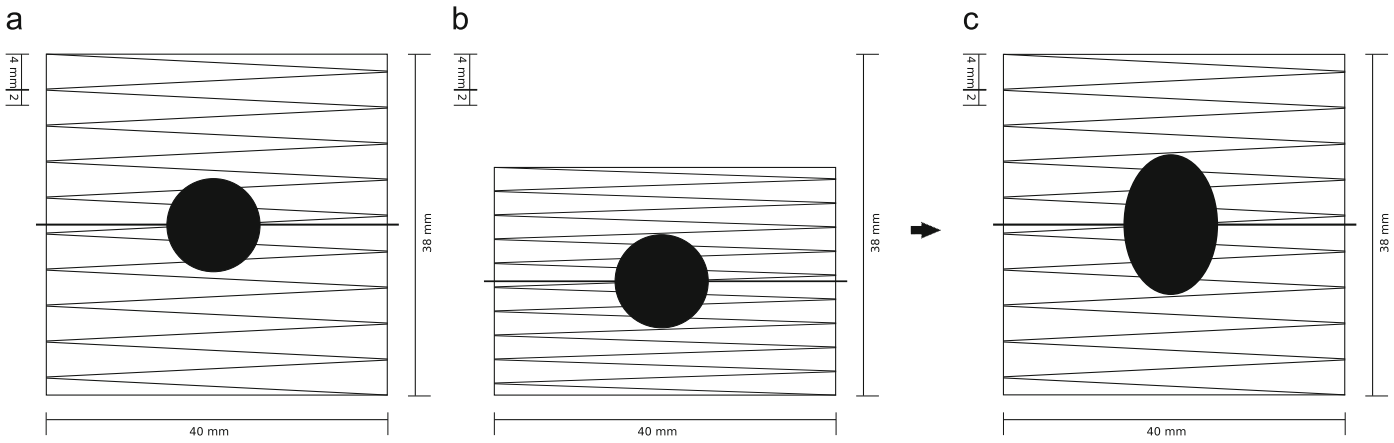

Fig. 5. Shows the means by which an elliptical charge cloud footprint was generated by the scaling of the cathode board dimensions within the model.

The 'maximum fractional excursion' is usually due to a few outliers rather than from the full range linearity, but is a good estimate of the worst possible performance. It is calculated as the maximum deviation of a detected position from the fit. Under many circumstances this is a poor estimate, often based on a few points with low statistic, or in a situation where some additional systematic effect caused a defective readout. Often repeating the point a couple of times proves that these points were, for example, 3 or 4 standard deviation random excursions which do not critically affect the detector (linearity) performance.

3.1. Circular model

The first detector model studied was that of a uniform (or top-hat) distribution of charge within a circle, and radii from 0.004 to 20 mm. Fig. 4 shows the χ_r^2 of the circular model fit to the experimental data over the parameter space of ion cloud radius. It is clear from this graph that there are six regions over the range of ion cloud radii that the model yields an improvement over the linear fit. The minimum χ_r^2 (2.06) is highlighted by an arrow and a dotted line, thus the best circle model was for an ion cloud with an apparent radius of about 8 mm (Fig. 3).

Closer inspection of the fractional residuals for this best circle model (Fig. 3) is important. Within the range of −11 to −2 mm the experimental residual from the model is centred about 0 with only statistical fluctuations remaining. The regions −2 to 3 mm and 3−9 mm of the model yield consistently positive and negative residuals, respectively. The outermost millimetre at each end of the active detection region demonstrates a limitation of the particular model output—here the ideal response is beginning to curve in the opposite direction from the experimental residual.

3.2. Elliptical model

It is expected that to first order a cloud will be circular, but as it sees different fields in orthogonal directions this could easily yield an elliptical shape. Hence the detector model was then extended to simulate a uniform distribution of charge within an ellipse through the introduction of an eccentricity parameter (ε). The eccentricity of the charge cloud describes the semi-major radius ($r_{\text{s-major}}$—along the axis of cathode sensitivity) as a percentage of the semi-minor radius ($r_{\text{s-minor}}$—along the anode sensitive dimension), $r_{\text{s-major}} = \varepsilon r_{\text{s-minor}}$.

Definition of an elliptical ion cloud in this way allowed for its simple implementation in the model by a scaling of the backgammon board dimensions as shown in Fig. 5. Fig. 5(a) shows a single circular charge cloud of the desired semi-major radius. Through scaling the anode sensitive dimension by the eccentricity parameter before projection of the charge cloud (Fig. 5(b)) the resulting charge footprint is equivalent to an ellipse of the desired dimensions (Fig. 5(c)).

The elliptical model was implemented for eccentricities of 10–500% and semi-major radii of 0.004–20 mm, however, many of the resulting simulations were discarded on the basis of being physically unreasonable. Fig. 6 shows the χ_r^2 of the remaining ellipse models fit to the experimental data. The red (solid) line shown indicates the χ_r^2 for the linear fit, such that any point below this line is an improvement over a straight line fit. As opposed to the six regions of improvement found for the circular model, with the elliptical model it is clear that the addition of the eccentricity parameter has lead to a much broader range of models with a low χ_r^2.

The best ellipse model ($\chi_r^2 = 1.94$) was for an ion cloud with an eccentricity of 60%, semi-major radius of about 6.1 mm, and semi-minor radius of about 10.2 mm (Fig. 7). A study of the experimental residual from the model shows a structure similar in features to that of the best circle model, with a few important improvements. The outermost millimetre at each end of the model output now follows the experimental data much more closely, so that the detector ranges between −12 and −2 mm and 9 to 12 mm are dominated only by statistical noise. The regions between −2 and 3 mm and 3 to 9 mm of the model still, however, demonstrate consistently positive and negative residuals.

3.3. Gaussian model

The circular and elliptical models discussed have been based on uniform distributions of charge. The detector simulation was modified to allow for a Gaussian distribution of charge onto the cathode board following each ionisation event. To achieve this, an approximation was made through the weighted sum of a range of circular ion clouds of uniform distribution, centred on the same coordinates, and parameterised by the Gaussian half-width-at-half-maximum (HWHM). The weighting of each circle was determined by the volume of an annulus formed within a solid Gaussian defined by the HWHM. This is an efficient and accurate partitional representation of a true Gaussian, to arbitrary level of approximation.

The number of circular elements used to make up each Gaussian distribution ranged from three to 101. Fig. 8 shows the χ_r^2 of an 11-element Gaussian model fit to the experimental data over the parameter space of ion cloud HWHM. The red (dashed) line shown indicates the χ_r^2 for the linear fit, such that any point below this line is an improvement over a straight line fit.

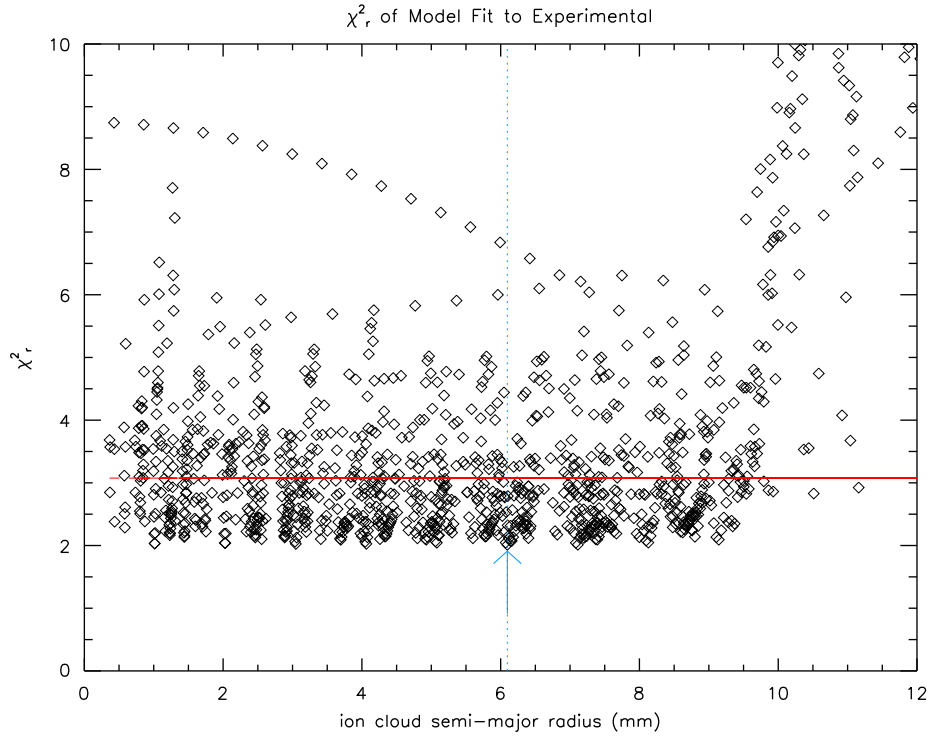

Fig. 6. Shows the χ^2_r of the model fit to the experimental data over the parameter space of ion cloud semi-major radius. Eccentricities of 10–500% are shown. The arrow highlights the minimum χ^2_r (1.94) for an elliptical ion cloud.

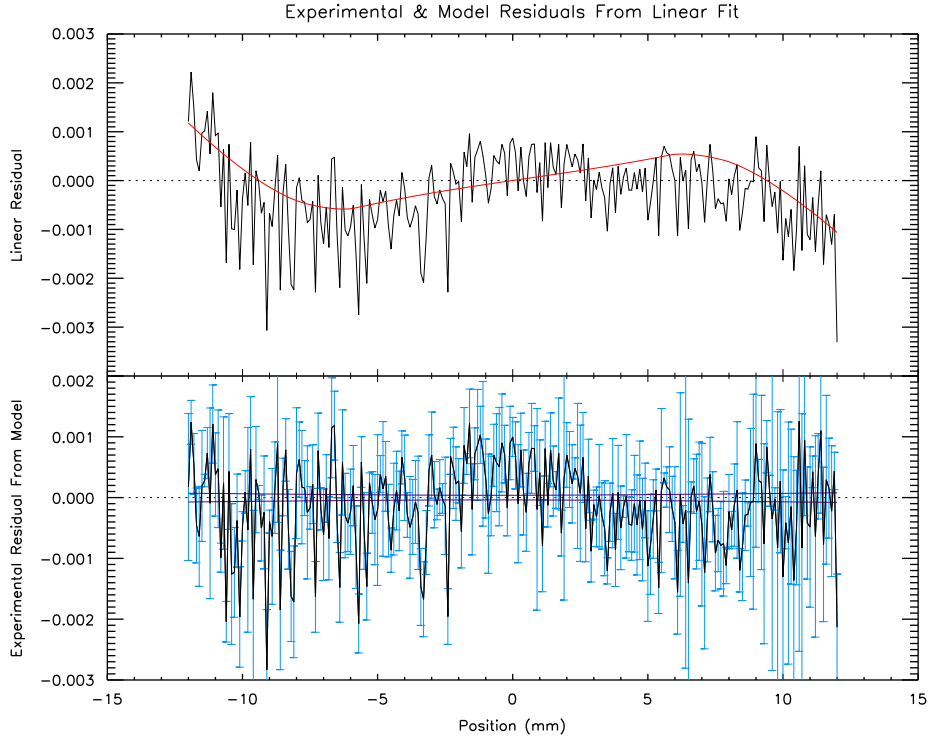

Fig. 7. Shows the fractional residuals for the best elliptical model ($\chi^2_r = 1.94$) with an eccentricity of 60%, semi-major radius of about 6.1 mm, and semi-minor radius of about 10.2 mm. The top graph shows the linear residual for both the experimental data and the model (smooth line). The lower graph shows the experimental residual from the model. Error bars are the standard percentage errors in the determined centroid position. The solid lines are the standard error envelope on the determined model fit.

The range in size over which the elements were chosen was also an important parameter of the model. Distributions within radii of 50–150% HWHM were used for the models shown in Figs. 8 and 9.

The best model constructed for a Gaussian distribution ($\chi^2_r = 1.95$) was for an 11-element Gaussian with approximately 2.6 mm HWHM and elements in the range of [50%, ... 150%]× HWHM. Fig. 9 shows the fractional residuals for this model.

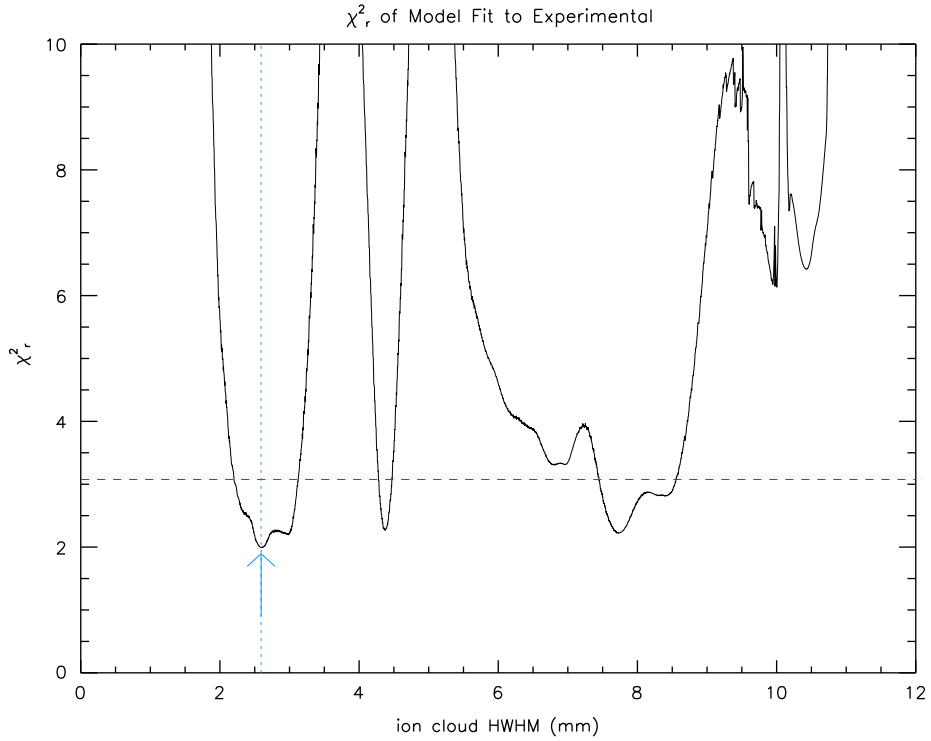

Fig. 8. Shows the χ^2_r of an 11-element Gaussian model fit to the experimental data over the parameter space of ion cloud HWHM. Elements were in the range of $[50\%, \ldots, 150\%] \times$ HWHM. The arrow highlights the minimum χ^2_r (1.95) for this model.

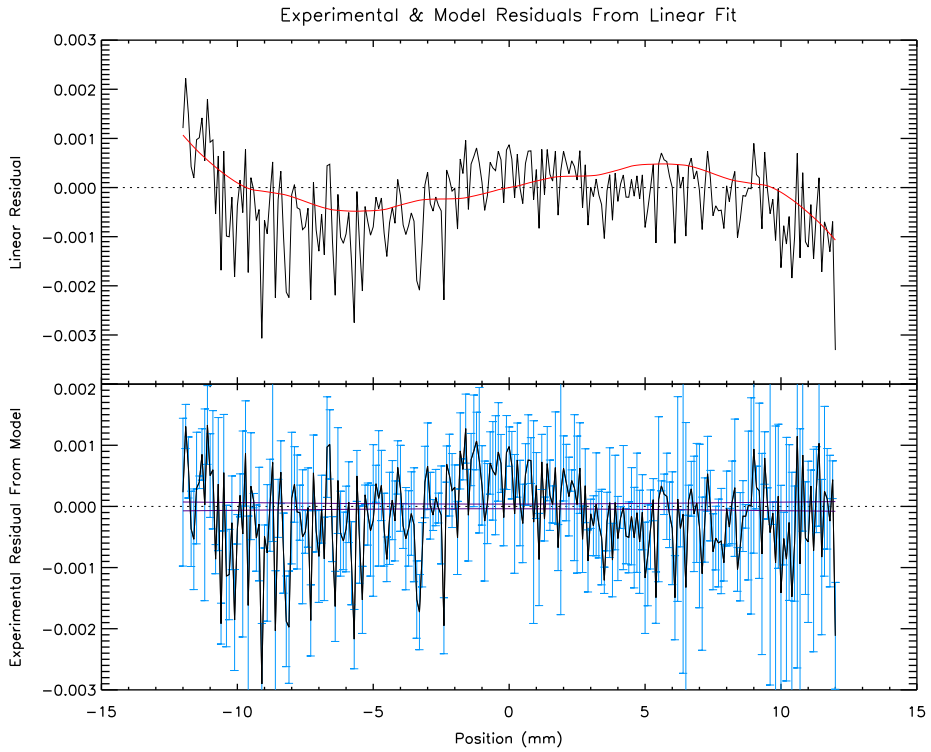

Fig. 9. Shows the fractional residuals for an 11-element Gaussian charge distribution with a HWHM of approximately 2.6 mm. The top graph shows the linear residual for both the experimental data and the model. The lower graph shows the experimental residual from the model (smooth line). Error bars are the standard percentage errors in the determined centroid position. The solid lines are the standard error envelope on the determined model fit.

This optimum has a structure not observed in earlier models. The oscillatory structure is due to the various elements of the distribution causing areas of non-ideal response (Section 2.5). As the number of elements within a distribution was increased, the Gaussian model output tended to that of the circular model. As such, the residual structure in Fig. 9 was dominated by an artifact of the finite element approximation used to generate the model. While this mapped the experimental data quite

closely, the result was not particularly robust nor physically insightful.

4. Results

For each of the three types of models presented herein (i.e. circular, elliptical and Gaussian model types), an expression for the linearity of the detector was determined, and found to be very close to that of an ideal linear fit, with $x' \in [0,1]$:

$$x' = (0.0199 \pm 4 \times 10^{-6})x(\text{mm}) + (0.505 \pm 3 \times 10^{-5}). \quad (5)$$

The linearity measures discussed in Section 3 were computed for each of these optimised models. As discussed above, the fitted gradient ($\Delta m/m$) and offset ($\Delta c/c$) are consistent and well-defined showing that the linear functional form is independent of the charge cloud modelling. Results are summarised in Table 1. The Gaussian, circle, and ellipse models show dramatic improvements over the simpler linear model for all (other) linearity measures.

Table 1 shows that the elliptical model best fits the experimental data collected, with a χ_r^2 of only 1.94. This model also exhibits the lowest percentage maximum error of fit at 0.00787% (or 3.2 μm) indicating that features spread across the active region of the detector can be resolved to a high level of accuracy.

Average deviations from fit were calculated to be only 0.0565% and 0.0566% for the Gaussian and ellipse models, respectively. This yields a good indication of the typical error on any single position determination within the detector. As the non-linearity of the translation stage is an order of magnitude better than the experimental results herein, a mechanical cause of the observed non-linearity is safely ignored.

The ellipse model exhibited the best regional differential non-linearity of only 0.0313% an improvement of 35% over the linear model. Likewise, the circle and Gaussian models showed improvements $> 30\%$. While a typical point-wise excursion (from statistical noise or random effects) might deviate by 0.001 in x', the deviation of a local region is much smoother and much of the structure is well-explained.

Finally, the maximum fractional excursion was minimised for the circle model at 0.272%. Whilst this measure is due to several outliers in the experimental data, which can skew the optimisation of the respective models and the final fit, the demonstrated improvement of 18% indicates that a significant component of the previous deviation was due to an inadequate model (i.e. the need for a representation of the charge cloud).

We note that the spatial range of the detector modelled does affect final optimisation and parametrisation. Modelling the central 20 mm instead of the full active 24 mm detector length yields a very similar slope and offset, and hence fitting uncertainty, but reduces the χ_r^2 by about 10%, and similarly reduces the regional differential non-linearity and maximum fractional excursion by approximately 10%. Since the improvement is moderately uniform, the results of the full fitting and linearity measures are presented.

Table 1
Summary of linearity measures by optimised model, fitted across the full active 24 mm detector length; values in bold are the best result for each linearity measure.

Measure	Linear	Gaussian	Circle	Ellipse
χ_r^2	3.075	1.948	2.055	**1.938**
% Maximum error of fit	0.009916	0.007892	0.008106	**0.007871**
Maximum error of fit (μm)	3.966	3.157	3.243	**3.148**
% Regional differential non-linearity	0.0484	0.0332	0.0336	**0.0313**
% Average deviation from fit	0.0670	**0.0565**	0.0583	0.0566
% Maximum fractional excursion	0.3307	0.2903	**0.2720**	0.2831

5. Conclusion

We have investigated the experimental linear residual of the backgammon-type MWPC, and shown the requirement for a representation of the charge cloud in modelling the ideal linear output of the detector. This paper does not theoretically prove a particular charge cloud shape, nor the ideal uniformity of that particular shape. It remains possible, for example, that key cloud radii might vary across a charge amplification device due to non-uniformities in construction; or that the radius might change with subtle changes in voltage or design; or that particular edge-effects might distort such a cloud shape.

Rather, it demonstrates that there is strong evidence for an approximately circular charge cloud distribution which is approximately uniform in a good typical implementation, and that this does indeed explain key systematic effects in the linearity function. This result thereby improves the potential determination of local structure in backgammon detectors, MWPCs and related charge amplification devices. Further, this paper demonstrates that highly accurate determination of position is possible with this detector type, and other related types, even if the resolution *per se* is not so high as e.g. CCD or other detectors. Of course, this accuracy is attained only with good statistics, and with appropriate modelling of detector response function.

References

[1] G. Charpak, R. Bouclier, T. Bressani, J. Favier, C. Zupancic, Nuclear Instruments and Methods 62 (1968) 262.
[2] C.T. Chantler, D. Paterson, L.T. Hudson, F.G. Serpa, J.D. Gillaspy, E. Takács, Physical Review A 62 (042501) (2000) 1.
[3] K. Assamagan, L. Baker, G. Bayatyan, R. Carlini, S. Danagoulian, T. Eden, K. Egiyan, R. Ent, H. Fenker, L. Gan, A. Gasparian, N. Grigoryan, Z. Greenwood, P. Gueye, O. Hashimoto, K. Johnston, C. Keppel, S. Knyazyan, S. Majewski, A. Margaryan, Y. Margaryan, G. Marikyan, J. Martoff, H. Mkrtchyan, L. Parlakyan, Y. Sato, R. Sawafta, N. Simicevic, V. Tadevosyan, T. Takahashi, L. Tang, G. Vartanyan, W. Vulcan, S. Wells, S. Wood, Nuclear Instruments and Methods in Physics Research A 426 (1999) 405.
[4] J. Fuzi, Measurement Science and Technology 19 (8) (2008).
[5] M. Irving, V. Lombardi, G. Piazzesi, M.A. Ferenczi, Nature 357 (1992) 156.
[6] C.T. Chantler, M.N. Kinnane, C.-H. Su, J.A. Kimpton, Physical Review A 73 (2005) 1.
[7] E. Gatti, A. Longoni, H. Okuno, P. Semenza, Nuclear Instruments and Methods 163 (1979) 83.
[8] V. Radeka, R.A. Boie, Nuclear Instruments and Methods 178 (1980) 543.
[9] F. Piuz, R. Roosen, J. Timmermans, Nuclear Instruments and Methods 196 (1982) 451.
[10] A.F. Barbosa, Nuclear Instruments and Methods in Physics Research A 371 (1996) 368.
[11] C. Martin, P. Jelinsky, M. Lampton, R.F. Malina, H.O. Anger, Review of Scientific Instruments 52 (7) (1981) 1067.
[12] J.F.C.A. Veloso, J.M.F. dos Santos, C.A.N. Conde, R.E. Morgado, X-ray Spectrometry 26 (1997) 237.
[13] P. Siritiprussamee, K. Fujita, H. Takahashi, H. Niko, K. Nishi, H. Toyokawa, M. Furusaka, T. Ino, S. Kishimoto, H.M. Shimizu, M. Kanazawa, Nuclear Instruments and Methods in Physics Research A 580 (2007) 1119.
[14] H. Natal da luz, J.F.C.A. Veloso, N.F.C. Mendes, J.M.F. dos Santos, J.A. Mir, Nuclear Instruments and Methods in Physics Research A 573 (2007) 191.
[15] A.T. Payne, J.A. Kimpton, M.N. Kinnane, C.T. Chantler, Measurement Science and Technology 20 (2009) 025601.
[16] R. Allemand, G. Thomas, Nuclear Instruments and Methods 137 (1976) 141.
[17] J.A. Kimpton, M.N. Kinnane, C.T. Chantler, Review of Scientific Instruments 77 (083102) (2006) 1.
[18] J.A. Kimpton, M.N. Kinnane, L.F. Smale, C.T. Chantler, L.T. Hudson, A. Henins, C.I. Szabo, J.D. Gillaspy, J.N. Tran, J.M. Pomeroy, E. Takács, B. Radics, Nuclear Instruments and Methods in Physics A 580 (2007) 246.
[19] G.G. Luther, P.L. Cowan, A. Henins, S. Brennan, Nuclear Instruments and Methods in Physics Research A 246 (1986) 537.
[20] T. Mizogawa, M. Sato, Y. Awaya, Nuclear Instruments and Methods in Physics Research A 366 (1995) 129.